RSC Advances

PAPER

View Article Online
View Journal | View Issue

Cite this: *RSC Adv.*, 2017, **7**, 121

F–Bi_4TaO_8Cl flower-like hierarchical structures: controlled preparation, formation mechanism and visible photocatalytic hydrogen production†

Muhammad Nawaz,[ab] Fangzhi Mou,[a] Leilei Xu,[a] Hao Tu[a] and Jianguo Guan*[a]

Received 11th October 2016
Accepted 13th October 2016

DOI: 10.1039/c6ra25046g

www.rsc.org/advances

Flower-like hierarchical structures of F–Bi_4TaO_8Cl were prepared *via* a facile hydrothermal route. The formation mechanism has been revealed to be a fluorine-mediated stepwise growth of F–Bi_4TaO_8Cl on the basis of the experimental results. The photocatalytic activity of the as-prepared product has been evaluated for hydrogen production by splitting water under visible light irradiation. It has been observed that flower-like hierarchical structures exhibited high photocatalytic activity compared with commercial Ta_2O_5, which may be ascribed to its unique hierarchical structure, greater light collection and harvesting ability, efficient charge separation and low band gap (2.25 eV). Our work provides a promising strategy for the controlled synthesis of visible-light driven photocatalysts for hydrogen production and can be potentially extended for the controlled synthesis and design of other semiconductors for energy production and environmental remediation.

Introduction

The production of hydrogen from solar light driven water splitting using semiconductor materials has received remarkable scientific and technological interest. It is an environmentally sound fuel source and a facile route towards the production of H_2. Considerable effort has been devoted to the purpose of seeking potential photocatalysts.[1–10] However, the current performance of this process is not adequate for its implementation on an industrial or large scale. Accordingly, there is a need for and a challenge to develop new visible-light driven photocatalysts to utilize sunlight efficiently for production of hydrogen.

The synthesis and design of nanostructured materials with controlled morphology and size has been getting interest as it provides an efficient way to regulate the different properties of materials such as magnetic, optical, electronic and catalytic properties.[11–13] The preparation of nanomaterials with controlled shape and size having reactive crystalline plane are critical for their catalytic properties and other applications.[14] Previously, we demonstrated that Ta_2O_5 flower-like hierarchical structures[15] and spheres[16] exhibited high photocatalytic hydrogen production activity than mesoporous or bulk Ta_2O_5. Therefore, development of an effective method for the synthesis of nanomaterials with controlled morphology and size is critical for photocatalytic hydrogen production.

Ta_2O_5 has received more attention due to its stability and excellent electronic configuration for water splitting.[17] Moreover, conduction band of Ta consists of Ta 5d which is more negative than Ti 3d, giving photogenerated electrons a strong reducing ability.[5,18] However, due to wide band gap (3.9 eV) its visible-light photocatalysis is limited.[19,20] Therefore, synthesis of Ta-based visible light-driven catalysts attracts considerable attention in photocatalytic hydrogen production.

Bismuth oxyhalides have been considered interesting material due to their electrical, optical and catalytic properties. The appropriate band gap and layered structures of such materials are responsible for their photocatalytic activities.[21–32] Zhang and co-workers found that BiOCl exhibited better activity than TiO_2 for the photocatalytic degradation of methyl orange.[33] However, wide band gap (3.46 eV) of BiOCl limited its visible light photocatalytic activity.[33] So, it is necessary to reduce the band gap of $Bi_xO_yX_z$ (X = Cl, Br, I) with some suitable metals to improve its visible light photocatalytic activity. Some bismuth-rich compounds such as $Bi_{24}O_{31}Br_{10}$ exhibited high photocatalytic activity for chromium (Cr) reduction and hydrogen production.[34] Similarly, $Bi_{24}O_{31}Cl_{10}$ and Bi_4TaO_8Cl also exhibited photocatalytic activity for dye degradation and it was prepared either by calcination of precursor or by electrolytic corrosion of bismuth (Bi) metal.[35–37] Currently, there is still challenge to prepare different stoichiometric bismuth oxychlorides nanoparticles with controlled-morphology through eco-friendly and cost effective route.

[a]*State Key Laboratory of Advanced Technology for Materials Synthesis and Processing, Wuhan University of Technology, Wuhan 430070, P. R. China. E-mail: guanjg@whut.edu.cn*

[b]*Department of Nano-Medicine Research, Institute for Research and Medical Consultations (IRMC), University of Dammam, Dammam 31441, Saudi Arabia*

† Electronic supplementary information (ESI) available. See DOI: 10.1039/c6ra25046g

To the best of our knowledge, there are no reports about the controlled preparation of F–Bi_4TaO_8Cl flower-like hierarchical structures with visible photocatalytic hydrogen production activity. In this work, we for the first time reported F–Bi_4TaO_8Cl flower-like hierarchical structures by a hydrothermal route. The structures, morphologies and optical properties of the as prepared product have been characterized. The photocatalytic activity of as prepared product was evaluated under visible light irradiation. A fluorine-mediated stepwise growth of F–Bi_4TaO_8Cl is rationally proposed based on control experiments.

Experimental details

Preparation of F–Bi_4TaO_8Cl flower-like hierarchical structures

Ta powder (99.95%), $BiCl_3$ (>98.0%), hydrofluoric acid (HF, 99.6%, 40 wt%), Ta_2O_5, isopropyl alcohol (99.7%) and ethanol (99.7%) were purchased from commercial suppliers and used without further purification. Deionized water was used in all reactions. 0.250 g $BiCl_3$ was dissolved in a mixture of aqueous HCl (1.5 M) and isopropyl alcohol (12.5 mL), followed by the addition of 0.020 g Ta powder and 0.2 mL HF. The resultant mixture was stirred and transferred into Teflon-line autoclave and heated in an electric oven at 150 °C for 24 h. After cooling to ambient temperature naturally, the white blackish precipitate obtained were centrifuged, washed several times with deionized water and ethanol and then dried at 60 °C for 12 h.

Characterization

X-ray powder diffraction (XRD, Rigaku, Japan, D/MAX-RB) was used to identify the phases of the products, using Cu Kα radiation ($\lambda = 1.5418$ Å) at scanning rate of 0.02° s^{-1} in the 2θ range from 10° to 80°. Field emission scanning electron microscope (FE-SEM; Hitachi, S-4800) was employed to observe the morphologies of the products at an acceleration voltage of 10.0 kV. The elemental composition was determined by a Horiba EX250 X-ray energy-dispersive (EDX) spectrometer associated with FE-SEM. Transmission electron microscopy (TEM), high resolution transmission electron microscopy (HRTEM) images and the corresponding selected area electron diffraction (SAED) patterns were captured on a JEM-2100F (Vender, Japan) with an accelerating voltage of 200 kV. UV-Vis diffuse reflectance spectra of the product was obtained on a diffuse reflectance UV-Vis spectrophotometer (UV-2550, Shimadzu, Japan) using $BaSO_4$ as a reference. X-ray photoelectron spectra (XPS) was recorded on an ultrahigh vacuum VG MultiLab 2000 X-ray photoelectron spectrometer (Thermo Electron Corporation, America), equipped with a monochromatic Mg Kα source and a charge neutralizer; the binding energies were referenced to the C 1s peaks at 284.6 eV of the surface adventitious carbon. Micromeritics ASAP 2020 nitrogen adsorption apparatus (USA) was employed for BET surface area determination. Before analysis, samples were degassed at 180 °C and surface area was determined by using N_2 adsorption data in the relative pressure (P/P_0) range of 0.05–0.3.

Photocatalytic hydrogen production

A closed gas circulation system was employed for photocatalytic hydrogen production; it was equipped with external-irradiation cell, under a 300 W xenon lamp. In a typical photocatalytic experiment, 30 mg of catalyst was dispersed ultrasonically in 80 mL aqueous lactic acid solution. Before irradiation, the suspension of the catalyst in reactor was evacuated for 15 minute to remove the dissolved gases and to ensure the reactor is in an anaerobic atmosphere. After the evacuation, the suspension was irradiated by Xe lamp as a light source. The generated hydrogen gas was determined *in situ* by a gas chromatogram (TECHCOMP, GC 7890-II) equipped with a TCD detector and a molecular sieve 5A column, using nitrogen as carrier gas.

Results and discussion

Morphology and structure characterization

The morphology and structure of the as-prepared product obtained at 150 °C were analyzed by FESEM, TEM, HRTEM and SAED. FESEM image of F–Bi_4TaO_8Cl prepared by hydrothermal method is presented in Fig. 1a, and the inset in Fig. 1a shows a high magnification FESEM image of a single flower. Fig. 1a clearly demonstrates that the product prepared at 150 °C is flower-like hierarchical structures with average diameter of 8 μm. Further careful observation indicates that each flower is composed of thin petals. TEM analysis has also been employed to further investigate the morphology and structure of as-prepared product. TEM image also indicates that the flower-like hierarchical structure is composed of thin petals (Fig. 1b). HRTEM analysis was conducted in order to get more insight into the crystal structure. HRTEM image shown in Fig. 1c indicates crystalline nature of the product. The interplanar spacing of 0.358 nm, coincides well with the [112] plane of monoclinic F–Bi_4TaO_8Cl. The inset in Fig. 1c shows the corresponding SAED pattern which further confirms the single crystalline structure.

The phase purity and crystal structure of as-prepared product were evaluated by X-ray diffraction (XRD) analysis. The XRD patterns of the product are presented in Fig. 1d, which can be indexed to monoclinic phase of F–Bi_4TaO_8Cl (JCPDS #86-2221). The sharp peaks indicate the well-crystalline nature of the product. The as-prepared product exhibits excellent stability under ambient conditions.

The XPS analysis of the as-prepared product was performed to confirm chemical state of the elements and composition of the product. Fig. 2a depicts the XPS pattern of the as-prepared product. The two peaks of Ta (Ta^{5+}) observed at 26.8 eV and 28.8 eV are assigned to Ta $4f_{7/2}$ and Ta $4f_{5/2}$ respectively (Fig. 2b). Similarly, two peaks are observed at 159.05 eV and 164.65 eV which can be assigned to Bi $4f_{5/2}$ and Bi $4f_{7/2}$ respectively; these are typical values for Bi^{3+} (Fig. 2c). Meanwhile, a peak at 199.10 eV is observed for Cl 2p (Fig. 2d). In Fig. 2e and f, the peaks at 529.75 eV and 685.40 eV correspond to O 1s and F 1s respectively. Based on these results, it can be concluded that the chemical composition of the as-prepared product is F–Bi_4TaO_8Cl.

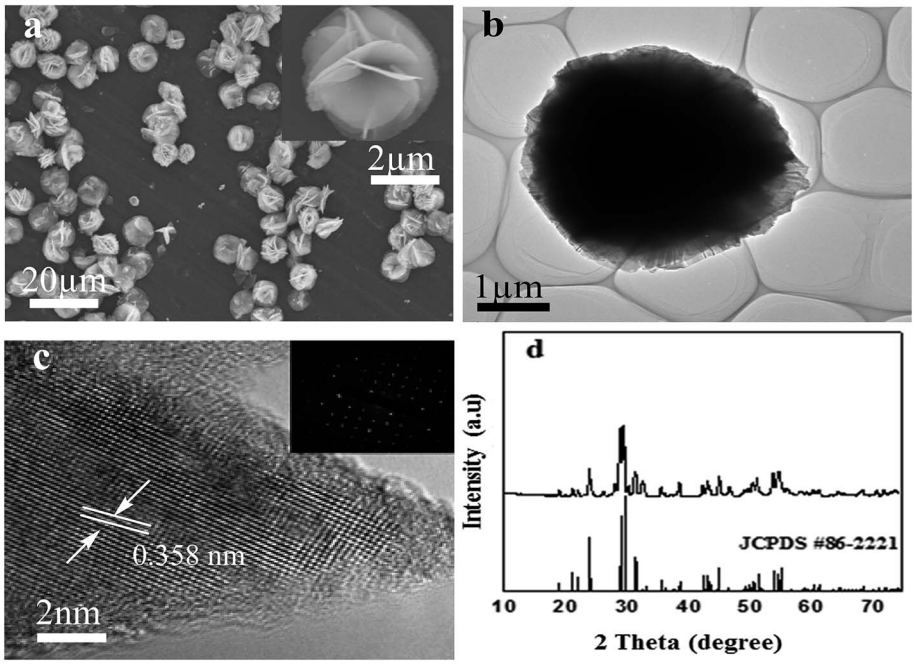

Fig. 1 FE-SEM images of F–Bi_4TaO_8Cl flower-like hierarchical structures (a) and a high magnification SEM image of a single F–Bi_4TaO_8Cl flower (the inset in a); TEM image of a single F–Bi_4TaO_8Cl flower (b) HRTEM image of a single F–Bi_4TaO_8Cl flower (c) the corresponding SAED pattern (the inset in c); XRD pattern of F–Bi_4TaO_8Cl flower-like hierarchical structures (d).

The EDX results of the as-prepared product is shown in Fig. 3a, which further confirms that the product consists of F, Bi, Ta, O and Cl and it coincides well with the chemical composition of the product (F–Bi_4TaO_8Cl). The EDX mapping of the product is presented in Fig. S1 (ESI†) which also confirms the chemical composition of the product.

Fig. 3b shows the N_2 adsorption–desorption isotherm and pore size distributions curve of the as-prepared product. The N_2 adsorption–desorption isotherm of the product is of type IV with H3 hysteresis loops according to IUPAC classification,[38] indicating the presence of mesopores (2–50 nm). Furthermore, isotherm reveals high absorption at high relatively pressure (*P*/

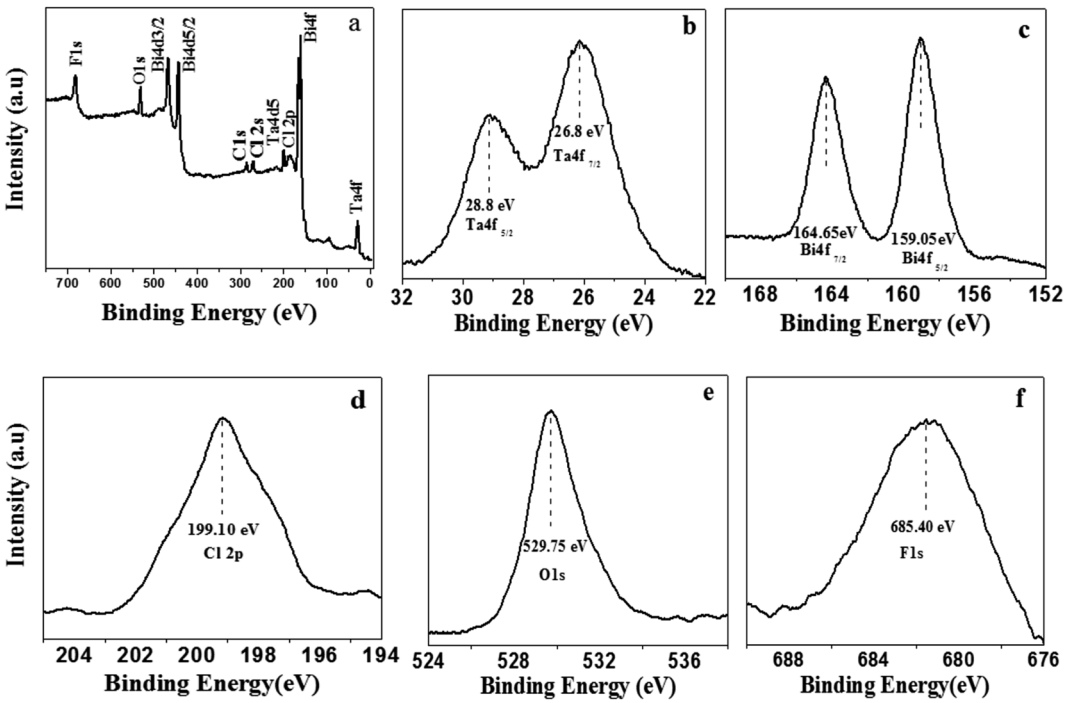

Fig. 2 XPS full (a), high magnified Ta 4f (b) Bi 4f (c) Cl 2p (d) O 1s (e) and F 1s (f) spectra of F–Bi_4TaO_8Cl flower-like hierarchical structures.

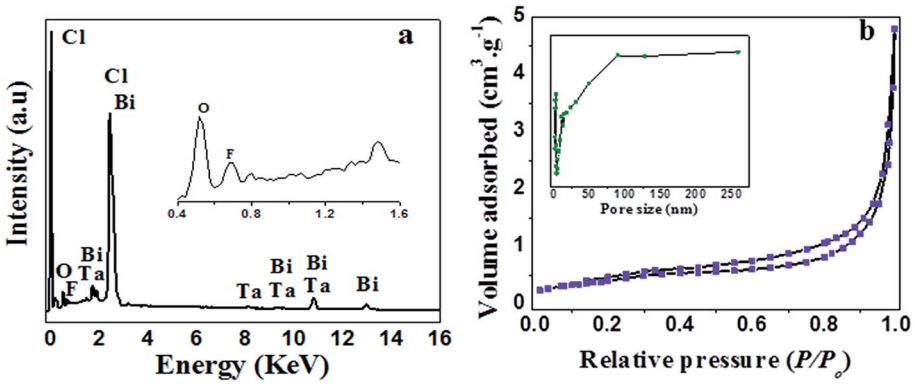

Fig. 3 EDX analysis (a) and N_2 adsorption–desorption analysis (b) of F–Bi_4TaO_8Cl flower-like hierarchical structures; the inset in (b) shows the pore size distribution.

P_0) range (around 1.0), indicating the formation of large mesopores and macropores (>50 nm).[39] The pore size distributions (insets in Fig. 3b) of the product shows a wide pore size distribution from 2–250 nm, which also confirms the existence of mesopores and macropores. BET surface area and textural properties of F–Bi_4TaO_8Cl are presented in Table 1.

Formation mechanism

To probe and elucidate the formation mechanism of the flower-like hierarchical structures, we performed time-dependent product formation experiments. The size and morphology of the products prepared at 150 °C for 1, 3, 6, 12 and 24 h were examined by FESEM analysis (Fig. 4a–e). The FESEM images (Fig. 4a–e) of the products obtained at various stages indicate the evolution of flower-like hierarchical morphology of the product. Initially, numerous plates like nuclei appear in the solution and then the crystal growth follows. As reaction proceeds further, these nuclei grow and consequently, the particles self-assembled to form nanoplates. These nanoplates attached together and assembled driven by van der Waals forces. The anisotropic electrostatic interactions arising from the dipole moment, combined with the binding affinity are also responsible for the formation of self-assembly of nanoplates. It has been widely investigated that self-assembly is controlled by attractive forces such as van der Waals force, hydrogen bonding and repulsive forces such as steric repulsion and electrostatic repulsion.[40–42] When the reaction was performed for 1 h, the resulting products are self-assembled underdeveloped aggregated nanoplates with an average diameter of 1 μm, as shown in Fig. 4a, while the inset displays the high magnification FESEM image of a single nanoplate. Upon increasing reaction time to 3 h, well-developed aggregated nanoplates are formed which can be observed from the FESEM image (Fig. 4b). As presented in Fig. 4b, nanoplates obtained after 3 h are 1 μm in diameter. After a specified reaction time of 6 h, anisotropic growth of nanoplates occurred determined by the lowest energy principle,[43] as a result nanoplates project out and grew further (Fig. 4c). After 6 h reaction, the diameter of nanoplates still

Table 1 Textural texture properties of F–Bi_4TaO_8Cl derived from the nitrogen adsorption–desorption isotherm data

Product	S_{BET} ($m^2\ g^{-1}$)	Pore size[a] (nm)	Pore volume[b] ($cm^3\ g^{-1}$)
Flower-like hierarchical structures	1.48	10.15	0.0037

[a] Pore size was estimated from BJH desorption determination. [b] Pore volume was determined by nitrogen adsorption volume at the relative pressure of 0.994.

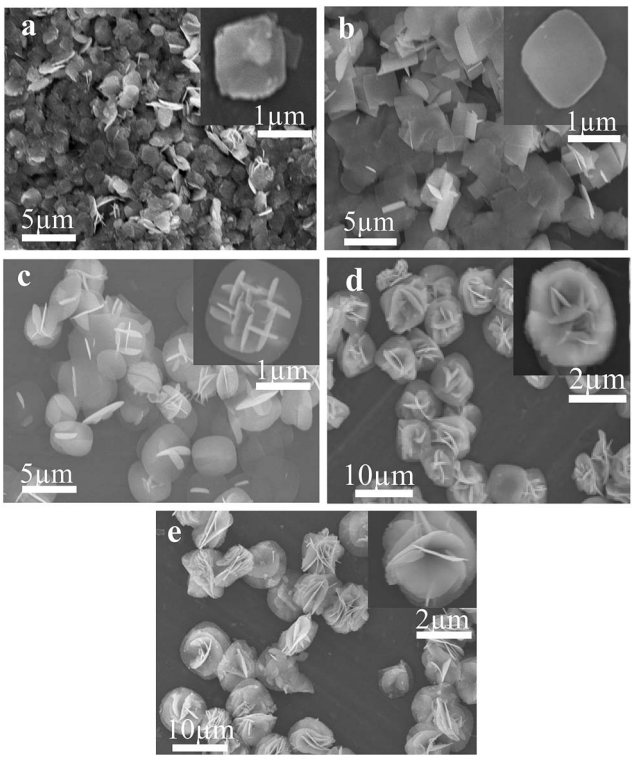

Fig. 4 SEM images of F–Bi_4TaO_8Cl flower-like hierarchical structures prepared at different reaction time of 1 h (a) 3 h (b) 6 h (c) 12 h (d) and 24 h (e) respectively.

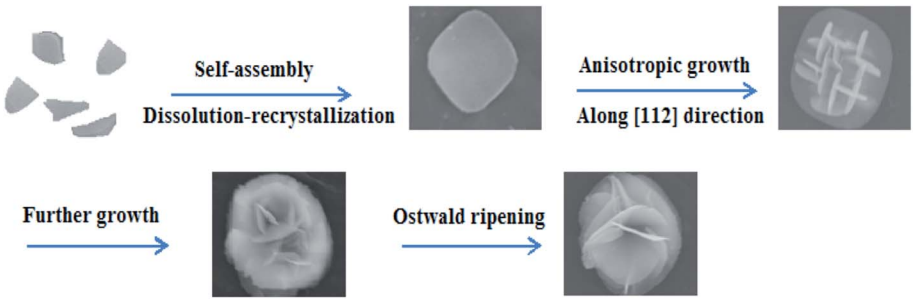

Fig. 5 Stepwise illustration for the formation mechanism of F–Bi_4TaO_8Cl flower-like hierarchical structures.

remains same as observed after 1 and 3 h (Fig. 4d). When the reaction time was further increased to 12 h, these nanoplates grew further and resulting in the formation of flower-like structures (Fig. 4d). Finally, when the reaction time was kept 24 h, as a result of Ostwald ripening, well-developed flower-like hierarchical structures are formed. These flower-like hierarchical structures having 8 μm average diameter are depicted in Fig. 4e. On the basis of the results discussed above, a feasible formation mechanism for flower-like hierarchical structure has been proposed and illustrated in Fig. 5.

The preferential growth direction of F–Bi_4TaO_8Cl flower-like hierarchical structure is governed by surface energy and magnetic anisotropic energy. When growth occurs along magnetic easy axis, magnetic anisotropic energy shows a minimum value[44,45] whereas surface energy has a lower value if the growth is along the normal direction of high energy facets. In our case, after the formation of nanoplates, the subsequent growth is subjected to a low rate. The minimization of magnetic anisotropic energy prevails over that of surface free energy and dominates the anisotropic growth of the subunits. The nanoplates grow along the [112] direction to acquire a low magnetic anisotropic energy in the presence of a relatively slow reaction rate. Consequently, tiny nanoplates project out and further grow into large plates. Finally, some nanoplates continue to grow as the reaction times increases, while tiny nanoplates disappear, possibly because of Ostwald ripening,[46,47] resulting in the formation of flower-like hierarchical structures (Fig. 5).

It is perceived that the presence of F on the surface of Bi_4TaO_8Cl has a significant role on the formation of nanoplates and might be responsible for the initial formation of well-developed nanoplates. Etching by F is initiated in the acidic medium and results in surface fluorination. It might be possible that F selectively interacts on the specific facet [112] of Bi_4TaO_8Cl and reduces surface energy and control the growth of nanostructures. In the present case, F is performing three different functions: to help to dissolve the Ta powder, to retard the hydrolysis of Bi precursor and to reduce the surface energy to promote the growth.[12,48] To explore the role of F in morphology formation, we carried out the reaction without the addition of HF and Ta, as it can be seen in Fig. S2a,† without the addition of HF and Ta, the product obtained is composed of irregular aggregated sheets. However, after the addition of HF in the reaction mixture, it results in the formation of well-developed nanoplates (Fig. S2b†). It implies the important role of HF in the controlled preparation of nanoplates. When the reaction was carried out both in the presence of HF and Ta, it results in the formation of flower-like hierarchical structures, which is probably due to further etching on Ta surface (Fig. S2c†).[12]

Photocatalytic hydrogen production

The photocatalytic hydrogen production activity of F–Bi_4TaO_8Cl flower-like hierarchical structures and commercial Ta_2O_5 were evaluated in aqueous lactic acid solution under visible light

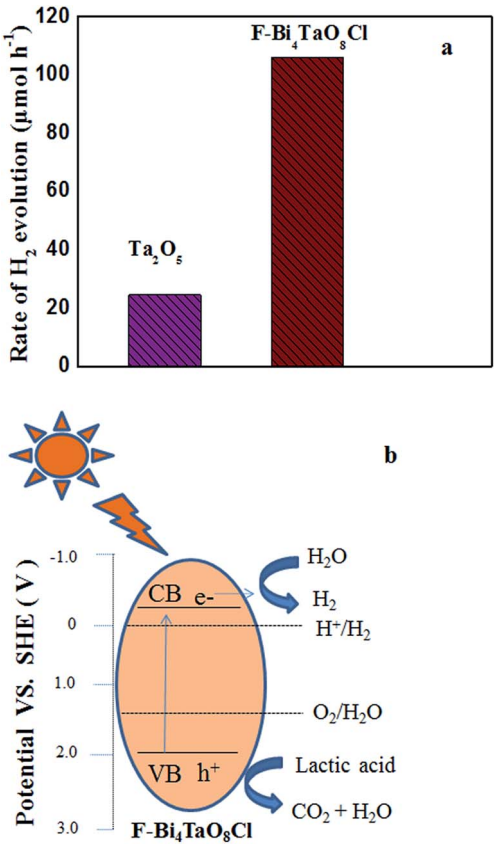

Fig. 6 Photocatalytic hydrogen production activity from aqueous lactic acid solution using Ta_2O_5 and F–Bi_4TaO_8Cl flower-like hierarchical structures under visible light irradiation (a) schematic illustration for the charge transfer and separation in F–Bi_4TaO_8Cl (b) under visible light irradiation.

irradiation without using any expensive cocatalysts such as Pt *etc.* As shown in Fig. 6a, commercial Ta_2O_5 exhibits very low photocatalytic activity (24.49 μmol h^{-1}) because of rapid recombination of photogenerated electrons and holes. Fig. 6a also indicates the photocatalytic activity of F–Bi_4TaO_8Cl flower-like hierarchical structures and it was observed 106 μmol h^{-1}. The higher photocatalytic activity of F–Bi_4TaO_8Cl than Ta_2O_5 can be ascribed to the fact that flower-like hierarchical structures offered more active sites due to their unique structures. Flower-like hierarchical structures allow more effective transport of the reactant molecules to get to the active sites on the framework walls, hence, enhancing the photocatalytic activity. The enhanced photocatalytic activity of flower-like hierarchical structures can also be attributed to its light absorption, reflection and multilight scattering efficiency, making the catalyst more efficient light harvester.[49,50] Energy level and electron transfer during hydrogen generation process is illustrated in Fig. 6b. Under visible light irradiation, F–Bi_4TaO_8Cl could be excited to generate the electrons (e^-) and holes (h^+) which are then separated. The excited electrons in the conduction band reduce water to hydrogen while holes in valence band of F–Bi_4TaO_8Cl oxidize water to oxygen. The DR-UV-Visible spectrum of F–Bi_4TaO_8Cl was measured and is presented in Fig. 7a. It can be clearly observed that flower-like hierarchical structures show strong absorption in the visible range with band gap of 2.25 eV. The flower-like hierarchical structures with narrow band gap are probable to collect and harvest not only high light efficiently and fast motion of charge carriers but also provides efficient transport pathways to reactant and product molecules, thus, resulting in high photocatalytic hydrogen production activity.[12]

As we discussed in formation mechanism, fluoride ion has significant role in controlled preparation. Additionally, fluoride ion also performs important role in photocatalytic hydrogen production. The surface fluoride ion can greatly reduce the recombination of photogenerated electrons and holes. Due to its strong electronegativity, fluoride ion can act as electron-trapping site to trap the photogenerated electrons by tightly holding the trapped electrons,[12] thus enhancing the hydrogen evolution rate. Here, flower-like hierarchical morphology of F–Bi_4TaO_8Cl, its low band gap (2.25 eV) and presence of fluoride ion are playing important role in visible light photocatalytic activity.

The evaluation of recycling and stability of catalysts is important in photocatalysis and for practical applications. We also investigated the stability of F–Bi_4TaO_8Cl by recycling the product; after three recycles no degradation was observed. However, minor changes in hydrogen production were observed, the insignificant changes in hydrogen production rate could be ascribed to consumption of sacrificial reagent in the reaction mixture. Thus these results indicate the stability of F–Bi_4TaO_8Cl under visible light irradiation (Fig. 7b).

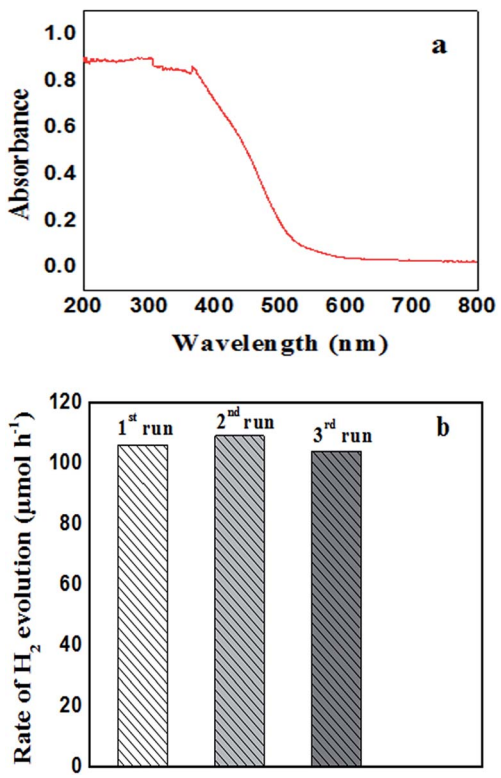

Fig. 7 UV-Vis DR spectra of F–Bi_4TaO_8Cl flower-like hierarchical structures (a) recycling run of F–Bi_4TaO_8Cl for hydrogen production under visible light irradiation (b).

Conclusions

We demonstrated the fabrication of F–Bi_4TaO_8Cl flower-like hierarchical structures by a facile hydrothermal method. A formation mechanism was proposed for the evolution of flower-like hierarchical structures based on the time-dependent experiments. The prepared product showed high hydrogen production activity under visible light irradiation. The facile, cost-effective and controlled preparation of this product is expected to be a potential and ideal candidate for applications in environmental remediation such as dyes and pesticides degradation.

Acknowledgements

This work was financially supported by the Fundamental Research Funds for the Central Universities (WUT: 2014-IV-063).

References

1 A. Fujishima and H. Honda, *Nature*, 1972, **238**, 37–38.
2 A. Kudo and Y. Miseki, *Chem. Soc. Rev.*, 2009, **38**, 253–278.
3 K. Domen, J. N. Kondo, M. Hara and T. Takata, *Bull. Chem. Soc. Jpn.*, 2000, **73**, 1307–1331.
4 K. Maeda and K. Domen, *J. Phys. Chem. C*, 2007, **111**, 7851–7861.
5 F. E. Osterloh, *Chem. Mater.*, 2008, **20**, 35–54.
6 L. Xu, C. Li, W. Shi, J. Guan and Z. Sun, *J. Mol. Catal. A: Chem.*, 2012, **360**, 42–47.
7 Y. Inoue, *Energy Environ. Sci.*, 2009, **2**, 364–386.

8 L. Yao, D. Wei, Y. Ni, D. Yan and C. Hu, *Nano Energy*, 2016, **26**, 248–256.
9 L. Yao, D. Wei, D. Yan and C. Hu, *Chem.–Asian J.*, 2015, **10**, 630–636.
10 M. Nawaz, *J. Photochem. Photobiol., A*, 2017, **332**, 326–330.
11 L. N. Lewis, *Chem. Rev.*, 1993, **93**, 2693–2730.
12 P. V. Kamat, *J. Phys. Chem. B*, 2002, **106**, 7729–7744.
13 Z. L. Wang, *Adv. Mater.*, 1998, **10**, 13–30.
14 K. B. Zhou, X. Wang, X. M. Sun, Q. Peng and Y. D. J. Li, *Catalysis*, 2005, **229**, 206–212.
15 J. Duan, W. Shi, L. Xu, G. Mou, Q. Xin and J. Guan, *Chem. Commun.*, 2012, **48**, 7301–7303.
16 C. Tao, L. Xu and J. Guan, *Chem. Eng. J.*, 2013, **229**, 371–377.
17 K. Sayama and H. Arakawa, *J. Photochem. Photobiol., A*, 1994, **77**, 243–245.
18 H. Kato and A. Kudo, *Chem. Phys. Lett.*, 1998, **295**, 487–492.
19 Y. Takahara, J. N. Kondo, T. Takata, D. L. Lu and K. Domen, *Chem. Mater.*, 2001, **13**, 1194–1199.
20 J. N. Kondo, M. Uchida, K. Nakajima, D. L. Lu, M. Hara and K. Domen, *Chem. Mater.*, 2004, **16**, 4304–4310.
21 M. A. Gondala, X. Chang, M. A. Ali, Z. H. Yamania, Q. Zhouand and G. Ji, *Appl. Catal., A*, 2011, **397**, 192–200.
22 J. Henle, P. Simon, A. Frenzel, S. Scholz and S. Kaskel, *Chem. Mater.*, 2007, **19**, 366–373.
23 X. Zhang, Z. Ai, F. Jia and L. Zhang, *J. Phys. Chem. C*, 2008, **112**, 747–753.
24 Y. F. Fang, W. H. Ma, Y. P. Huang and G. W. Cheng, *Chem.–Eur. J.*, 2013, **19**, 3224–3229.
25 L. Ye, C. Gong, J. Liu, L. Tian, T. Peng, K. Deng and L. Zan, *J. Mater. Chem.*, 2012, **22**, 8354–8360.
26 J. Cao, B. Y. Xu, H. L. Lin, B. D. Luo and S. F. Chen, *Catal. Commun.*, 2012, **26**, 204–208.
27 Y. Feng, L. Li, J. Li, J. Wang and L. Liu, *J. Hazard. Mater.*, 2011, **192**, 538–544.
28 X. Xiao, R. Hao, M. Liang, X. X. Zuo, J. M. Nan, L. S. Li and W. D. Zhang, *J. Hazard. Mater.*, 2012, **233–234**, 122–130.
29 J. Xu, W. Meng, Y. Zhang, L. Li and C. Guo, *Appl. Catal., B*, 2011, **107**, 355–362.
30 Y. Fan, Y. Huang, J. Yang, P. Wang and G. Cheng, *Environ. Sci. Technol.*, 2011, **45**, 1593–1600.
31 F. Dong, Y. J. Sun, M. Fu, Z. B. Wu and S. C. Lee, *J. Hazard. Mater.*, 2012, **219–220**, 26–34.
32 L. Ye, J. Liu, C. Gong, L. Tian, T. Peng and L. Zan, *ACS Catal.*, 2012, **2**, 1677–1683.
33 K. L. Zhang, C. M. Liu, F. Q. Huang and W. D. Wang, *Appl. Catal., B*, 2006, **68**, 125–130.
34 J. Shang, W. C. Hao, X. J. Lv, T. M. Wang, X. L. Wang, Y. Du, S. X. Dou, T. F. Xie, D. J. Wang and J. O. Wang, *ACS Catal.*, 2014, **4**, 954–961.
35 F. T. Li, Q. Wang, X. J. Wang, B. Li, Y. J. Hao, R. H. Liua and D. S. Zhao, *Appl. Catal., B*, 2014, **150–151**, 574–584.
36 G. Che, G. L. Fang and G. D. Tang, *Mater. Res. Bull.*, 2013, **48**, 1256–1261.
37 S. M. B. Swetha and G. S. Nalini, *RSC Adv.*, 2013, **3**, 14371–14378.
38 K. S. W. Sing, D. H. Everett, R. A. W. Haul, L. Moscou, R. A. Pierotti, J. Rouquerol and T. Siemieniewska, *Pure Appl. Chem.*, 1985, **57**, 603–619.
39 D. V. Bavykin, V. N. Parmon, A. A. Lapkin and F. C. Walsh, *J. Mater. Chem.*, 2004, **14**, 3370–3377.
40 H. Zhang and D. Y. Wang, *Angew. Chem., Int. Ed.*, 2008, **47**, 3984–3987.
41 S. H. Lee, Y. S. Her and E. Matijevic, *J. Colloid Interface Sci.*, 1997, **186**, 193–202.
42 Z. Y. Tang, Z. L. Zhang, Y. Wang, S. C. Glotzer and N. A. Kotov, *Science*, 2006, **314**, 274–278.
43 J. Ye, Q. W. Chen, H. P. Qi and N. Tao, *Cryst. Growth Des.*, 2008, **8**, 2464–2468.
44 D. F. Wan and X. L. Ma, *Magnetic Physics*, Publishing House of Electronics Industry, Beijing, 1999.
45 C. Burda, X. B. Chen, R. Narayanan and M. A. El-Sayed, *Chem. Rev.*, 2005, **105**, 1025–1102.
46 J. Li and H. C. Zeng, *J. Am. Chem. Soc.*, 2007, **129**, 15839–15847.
47 H. G. Yang and H. C. Zeng, *J. Phys. Chem. B*, 2004, **108**, 3492–3495.
48 H. G. Yang, C. H. Sun, S. Z. Qiao, J. Zou, G. Liu, S. C. Smith, H. M. Cheng and G. Q. Lu, *Nature*, 2008, **453**, 638–642.
49 X. Wang, J. Yu, C. Ho, Y. Hou and X. Fu, *Langmuir*, 2005, **21**, 2552–2559.
50 B. Fang, A. Bonakdarpour, K. Reilly, Y. Xing, F. Taghipour and D. P. Wilkinson, *ACS Appl. Mater. Interfaces*, 2014, **6**, 15488–15498.